Self-consistent calculation of nuclear photoabsorption cross section: Finite amplitude method with Skyrme functionals in the three-dimensional real space

Tsunenori Inakura,[1,2] Takashi Nakatsukasa,[2,1] and Kazuhiro Yabana[1,2]

[1] *Center for Computational Sciences, University of Tsukuba, Tsukuba 305-8571, Japan*
[2] *Theoretical Nuclear Physics Laboratory, RIKEN Nishina Center, Wako, 351-0198, Japan*

The finite amplitude method (FAM), which we have recently proposed (T. Nakatsukasa, T. Inakura, and K. Yabana, Phys. Rev. C**76**, 024318 (2007)), simplifies significantly the fully self-consistent RPA calculation. Employing the FAM, we are conducting systematic, fully self-consistent response calculations for a wide mass region. This paper is intended to present a computational scheme to be used in the systematic investigation and to show the performance of the FAM for a realistic Skyrme energy functional. We implemented the method in the mixed representation in which the forward and backward RPA amplitudes are represented by indices of single-particle orbitals for occupied states and the spatial grid points for unoccupied states. We solve the linear response equation for a given frequency. The equation is a linear algebraic problem with a sparse non-hermitian matrix, which is solved with an iterative method. We show results of the dipole response for selected spherical and deformed nuclei. The peak energies of the giant dipole resonance agree well with measurements for heavy nuclei, while they are systematically underestimated for light nuclei. We also discuss the width of the giant dipole resonance in the fully self-consistent RPA calculation.

PACS numbers:

I. INTRODUCTION

Nuclear density-functional theory has been successful for a systematic description of ground-state properties such as binding energies, density distributions, deformations, and so on. In the last decade, systematic density-functional calculations for a whole nuclear chart have come to be an ordinary work where a variety of energy functionals are employed [1, 2]. One of the major goals of such systematic investigations is an assessment and an improvement of the energy functionals. A rapid progress of experimental research on unstable nuclei also necessitates a development of an accurate and universal energy functional that describes nuclei far from the stability line. These efforts ultimately aim to establish a theory with a high predictive power and high accuracy.

The nuclear density-functional theory is also capable of describing excited state properties. The random-phase approximation (RPA), which is derived by linearizing the time-dependent mean-field equation [3], describes the nuclear excitation as a small-amplitude oscillations around the ground state. It has been successful for describing both giant resonances and low-lying modes of excitations. In practical calculations, the RPA equation has been solved mostly in the matrix diagonalization scheme. In these calculations, it was common to ignore a part of the residual interaction, sacrificing the full self-consistency. This is because the inclusion of the full residual interaction for a realistic interaction involves a cumbersome and complicated task. Recently several groups have reported fully self-consistent RPA calculations [4–8]. However, they are mostly restricted to spherical nuclei. There are a few recent attempts for deformed nuclei [9–14].

Recently, we have proposed a new method to solve the RPA equation, the finite amplitude method (FAM) [15]. The FAM allows us to evaluate the fully self-consistent residual fields as a finite difference, employing a computational code for the *static* mean-field Hamiltonian alone with a minor modification. In Ref.[15], we showed that the FAM works accurately in solving the RPA equation for a deformed nucleus ^{20}Ne with a simplified interaction.

Employing the FAM, we are undertaking a systematic investigation of nuclear response for a wide mass region ($A \leq 100$). The purpose of this paper is to explain the implementation of the FAM with a realistic Skyrme functional to be employed in such systematic investigation.

Our scheme is summarized as follows:

1. Fully self-consistent RPA calculation. The identical Skyrme energy functional is used for both ground state and linear response calculations, including spin-orbit, Coulomb, and time-odd-density terms.

2. Applicable to deformed nuclei. To describe any kind of deformation, we employ a three-dimensional (3D) real-space grid representation.

3. Linear response equation is solved employing an iterative method for the external field with a given frequency.

We employ a mixed representation in which the RPA forward and backward amplitudes are described with orbital indices for occupied single-particle states and the 3D grid-points for unoccupied states. In the mixed representation, the RPA equation is a linear algebraic equation with a sparse, non-hermitian matrix. The dimensionality is typically an order of 10^6. We will examine and compare performance of different solvers for the linear algebraic problem, and demonstrate that the FAM works

excellently for realistic calculations with complicated energy functionals.

At present, we ignore the pairing terms. The pairing effects will not be important for high-lying negative-parity excitations such as the dipole excitation which we investigate in this paper. However, the pairing may have significant effects on the low-lying modes such as quadrupole excitations. An extension to include the pairing is now under study. In order to treat the particle escape, we need to impose a continuum boundary condition [16]. Although it can be managed in the present scheme [14], the accurate description requires a heavy computational task. For a systematic investigation which we pursue, we must find a compromise between the accuracy of the calculation and the computational feasibility. We will approximately take into account the continuum effects by solving the RPA equation inside a 3D spherical box of a large radius.

This paper is organized as follows. In Sec. II, we review formalism of the FAM. The numerical details and the related techniques are discussed in Sec. II C. To show the accuracy of the method, the FAM results are compared with the fully self-consistent RPA results in the conventional diagonalization scheme. Calculated results are shown in Sec. III for selected nuclei in light and heavy mass regions. Convergence with respect to the model space, dependence on the functionals will be discussed. Finally, our fully self-consistent RPA results are compared with experimental data. Conclusions are presented in Sec. IV.

II. LINEAR-RESPONSE CALCULATION WITH A SKYRME FUNCTIONAL

A. Linear response equation in the mixed representation

Under a weak, time-dependent external field $V_{\rm ext}(t)$, the transition density $\delta\rho(t)$ follows the equation ($\hbar = 1$)

$$i\frac{\mathrm{d}}{\mathrm{d}t}\delta\rho(t) = [h_0\,,\,\delta\rho(t)] + [V_{\rm ext}(t) + \delta h(t)\;\rho_0]\,, \qquad (1)$$

where ρ_0 and $h_0 = h[\rho_0]$ are the ground-state density and the single-particle Hamiltonian, respectively. $\delta h(t)$ is a residual field induced by density fluctuation, $h[\rho(t)] = h_0 + \delta h(t)$. Assuming that $\delta\rho(t)$, $V_{\rm ext}(t)$, and $\delta h(t)$ oscillate with a frequency ω like $\delta\rho(t) = \delta\rho(\omega)e^{-i\omega t} + \delta\rho^\dagger(\omega)e^{i\omega t}$, Equation (1) is recast to

$$\omega\delta\rho(\omega) = [h_0,\,\delta\rho(\omega)] + [V_{\rm ext}(\omega) + \delta h(\omega), \rho_0]\,. \qquad (2)$$

Since $\delta\rho(\omega)$ is not necessarily hermitian, we need forward and backward amplitudes, $|X_i(\omega)\rangle$ and $|Y_i(\omega)\rangle$, to express the transition density $\delta\rho(\omega)$.

$$\delta\rho(\omega) = \sum_{i=1}^{A}\left\{|X_i(\omega)\rangle\langle\phi_i| + |\phi_i\rangle\langle Y_i(\omega)|\right\}, \qquad (3)$$

where $A = N + Z$ is the mass number of the nucleus and the orbitals ϕ_i are occupied orbitals in the ground state, $h_0|\phi_i\rangle = \epsilon_i|\phi_i\rangle$ ($i = 1, \cdots, A$). Substituting this expression into Eq. (2), we obtain the RPA linear-response equation:

$$\begin{aligned}
\omega|X_i(\omega)\rangle &= (h_0 - \epsilon_i)\,|X_i(\omega)\rangle \\
&\quad + \hat{P}\left\{V_{\rm ext}(\omega) + \delta h(\omega)\right\}|\phi_i\rangle, \quad (4)\\
-\omega\langle Y_i(\omega)| &= \langle Y_i(\omega)|\,(h_0 - \epsilon_i) \\
&\quad + \langle\phi_i|\left\{V_{\rm ext}(\omega) + \delta h(\omega)\right\}\hat{P}, \quad (5)
\end{aligned}$$

where $\hat{P}$ denotes the projector onto the particles space, $\hat{P} = 1 - \sum_{i=1}^{A}|\phi_i\rangle\langle\phi_i|$. In Eqs. (4) and (5), if we expand $\delta h(\omega)$ with respect to the forward and backward amplitudes in the linear order, we obtain the well-known $A - B$ matrix form of the RPA equations [3, 15]. When the single-particle Hamiltonian and the external field are both local in coordinate space, we may write Eqs. (4) and (5) conveniently in the coordinate representation,

$$\begin{aligned}
\omega X_i(\xi,\omega) &= (h_0(\xi) - \epsilon_i)\,X_i(\xi,\omega) \\
&\quad + \hat{P}\left\{V_{\rm ext}(\xi,\omega) + \delta h(\xi,\omega)\right\}\phi_i(\xi), \quad (6)\\
-\omega Y_i^*(\xi,\omega) &= [(h_0(\xi) - \epsilon_i)\,Y_i(\xi,\omega) \\
&\quad + \hat{P}\left\{V_{\rm ext}^\dagger(\vec{\xi},\omega) + \delta h^\dagger(\xi,\omega)\right\}\phi_i(\xi)\Big]^*, \quad (7)
\end{aligned}$$

where the coordinate ξ may contain the spin index σ as well as the spatial coordinate $\vec{r}$, $\xi = (\vec{r},\sigma)$. This is often referred to the mixed representation [12, 13, 17]. It should be noted that, since $\delta h(\omega)$ has a linear dependence on $X_i(\omega)$ and $Y_i^*(\omega)$, this is an inhomogeneous linear algebraic equation of the form $\mathbf{A}\vec{x} = \vec{b}$ where $\vec{x} \equiv (X_i(\xi,\omega), Y_i^*(\xi,\omega))$ [15]. In our implementation, we employ the grid representation of the 3D Cartesian-coordinate space. Denoting the number of the spatial grid points as $N_{\vec{r}}$, the dimension of the vector $\vec{x}$ is $N_{\vec{r}} \times A \times 2 \times 2$ (a factor of two for the forward and backward amplitudes and another factor of two for the spin degrees of freedom). $N_{\vec{r}}$ is order of 10,000 (see Sec. II C 1). For systems described by local potentials, we need not introduce any further truncations in the particle space. In the 3D grid representation the treatment of the particle escape is better controlled than that in other representations, for example, the harmonic-oscillator-basis representation.

B. Finite amplitude method (FAM)

If we write the residual field $\delta h(\xi,\omega)$ explicitly with the forward $X_i(\xi,\omega)$ and backward $Y_i(\xi,\omega)$ amplitudes, it requires us to calculate the residual two-body kernel, $v(\xi,\xi') = \delta h(\xi,\omega)/\delta\rho(\xi')$. However, if one employs a realistic energy functional, the explicit construction of the residual two-body kernel involves a complicated coding and a large numerical task. For this reason, it has been a common procedure to approximate or ignore a part of the

residual interaction in most RPA calculations. For example, the velocity-dependent terms are sometimes replaced with the Landau-Migdal interaction. The spin-spin, the spin-orbit, and the Coulomb residual interactions are often neglected.

To achieve a fully self-consistent RPA calculation, we believe that the FAM [15] is one of the simplest methods, at least, with respect to programming. In the FAM, we evaluate $\delta h(\xi,\omega)$ directly from the ground state Hamiltonian $h[\rho]$ by the finite difference method, thus avoiding an explicit construction of the residual two-body kernel. In this section, we recapitulate the essence of the FAM. Readers are referred to Ref. [15] for details.

The residual field $\delta h(\xi,\omega)$ depends linearly on $\delta\rho(\omega)$: $\delta h(\omega) = \partial h/\partial\rho|_{\rho=\rho_0}\cdot\delta\rho(\omega)$. In the first oder with respect to a small parameter η, we have

$$h_0 + \eta\delta h(\omega) = h\left[\rho_0 + \eta\delta\rho(\omega)\right] \equiv h\left[\tilde{\rho}_\eta(\omega)\right]. \tag{8}$$

Here, the one-body *pseudo-density* operator $\tilde{\rho}_\eta(\omega) \equiv \rho_0 + \eta\delta\rho(\omega)$ is a non-hermitian operator expressed with bra and ket vectors as follows:

$$\tilde{\rho}_\eta(\omega) = \sum_i \left(|\phi_i\rangle + \eta|X_i(\omega)\rangle\right)\left(\langle\phi_i| + \eta\langle Y_i(\omega)|\right). \tag{9}$$

In the linear order in η, Equation (8) is expressed as

$$\delta h(\omega) = \frac{1}{\eta}\left(h\left[\tilde{\rho}_\eta(\omega)\right] - h_0\right). \tag{10}$$

This is the basic result of the FAM. Equation (10) indicates that $h\left[\tilde{\rho}_\eta(\omega)\right]$ can be evaluated in the same manner as in $h_0 = h[\rho_0]$, with a replacement of the ordinary densities with the *pseudo-densities*: For instance, the *pseudo-local-density*, *pseudo-kinetic-density*, and *pseudo-current-density* are given by

$$\begin{aligned}
\tilde{\rho}_\eta(\vec{r}) &= \sum_i\sum_\sigma \psi_i^*(\xi)\varphi_i(\xi),\\
\tilde{\tau}_\eta(\vec{r}) &= \sum_i\sum_\sigma \nabla\psi_i^*(\xi)\cdot\nabla\varphi_i(\xi),\\
\vec{\tilde{j}}_\eta(\vec{r}) &= \frac{1}{2i}\sum_i\sum_\sigma\{\psi_i^*(\xi)\nabla\varphi_i(\xi) - (\nabla\psi_i^*(\vec{r}))\varphi_i(\vec{r})\},
\end{aligned} \tag{11}$$

respectively, where $\varphi_i = \phi_i + \eta X_i(\omega)$ and $\psi_i = \phi_i + \eta Y_i(\omega)$. The spin-dependent pseudo-densities are also defined in the same manner. Once $X_i(\omega)$, $Y_i(\omega)$, and η are given, the pseudo-densities are calculated as in Eq. (11).

Equations (6) and (7) are the linear algebraic equation of the form, $\mathbf{A}\vec{x} = \vec{b}$. Here,

$$\vec{x} = \begin{pmatrix} X_i(\xi,\omega)\\ Y_i^*(\xi,\omega)\end{pmatrix}, \qquad \vec{b} = \begin{pmatrix} -V_{\rm ext}(\xi,\omega)\phi_i(\xi)\\ -\{V_{\rm ext}(\xi,\omega)\phi_i(\xi)\}^*\end{pmatrix}. \tag{12}$$

To solve Eqs. (6) and (7), we utilize the iterative scheme, as described below. In the iterative scheme, we need not construct the matrix elements of $\mathbf{A}$ explicitly but always evaluate $\mathbf{A}\vec{x}$ employing the FAM for a given vector $\vec{x}$.

$$\mathbf{A}\vec{x} = \begin{pmatrix} (h_0(\xi) - \epsilon_i - \omega)X_i(\xi,\omega) + \delta h(\xi,\omega)\phi_i(\xi)\\ \left\{(h_0(\xi) - \epsilon_i + \omega^*)Y_i(\xi,\omega) + \delta h^\dagger(\xi,\omega)\phi_i(\xi)\right\}^*\end{pmatrix}, \tag{13}$$

where $\delta h(\xi,\omega)\phi_i(\xi)$ is calculated using Eq. (10) and $\delta h^\dagger(\xi,\omega)\phi_i(\xi)$ using the same equation but $\tilde{\rho}_\eta$ replaced by $\tilde{\rho}_\eta^\dagger$. To find a solution of Eqs. (6) and (7), we employ extensions of the conjugate gradient method for linear algebraic equations involving a non-hermitian matrix. In the literature, quite a few solvers for linear algebraic equations involving a non-hermitian matrix have been developed. However, we find only a few methods work for the present problem. We will discuss it in Sec. II C.

In order to calculate the strength function for a given one-body operator F, we adopt an external field of $V_{\rm ext}(t) = \eta F e^{-i\omega t} + \eta^* F^\dagger e^{i\omega t}$. Then, the transition strength is expressed with the forward and backward amplitudes,

$$\begin{aligned}
\frac{dB(E;F)}{dE} &\equiv -\frac{1}{\pi}{\rm Im}\sum_i\left\{\langle\phi_i|F^\dagger|X_i(\omega)\rangle + \langle Y_i(\omega)|F^\dagger|\phi_i\rangle\right\}\\
&= \sum_n |\langle n|F|0\rangle|^2\,\delta(E - E_n),
\end{aligned} \tag{14}$$

for a real frequency $\omega = E$. Here, $|n\rangle$ are energy eigenstates of the total system. In the following calculations, we use complex frequencies with a finite imaginary part, $\omega = E + i\gamma/2$. Then, the transition strength becomes

$$\frac{dB(E;F)}{dE} = \frac{\gamma}{2\pi}\sum_n\left\{\frac{|\langle n|F|0\rangle|^2}{\left(E - E_n\right)^2 + \left(\gamma/2\right)^2} - \frac{|\langle n|F^\dagger|0\rangle|^2}{\left(E + E_n\right)^2 + \left(\gamma/2\right)^2}\right\} \tag{15}$$

The second term in the right hand side is not important, if $\gamma \ll E + E_n$. For an hermitian operator F, this leads to

$$\frac{dB(E;F)}{dE} = \frac{2E\gamma}{\pi}\sum_n \frac{\tilde{E}_n|\langle n|F|0\rangle|^2}{\left(E^2 - \tilde{E}_n^2\right)^2 + E^2\gamma^2}, \tag{16}$$

where $\tilde{E}_n^2 \equiv E_n^2 + \gamma^2/4$.

In this article, we consider an electric dipole operator for F.

$$D_z^{E1} = \frac{N}{A}e\sum_{p=1}^{Z} z_p - \frac{Z}{A}e\sum_{n=1}^{N} z_n, \tag{17}$$

and similar operators for D_x^{E1} and D_y^{E1}. The photoabsorption cross section in the dipole approximation is given as follows [18],

$$\sigma_{\rm abs}(E) = \frac{4\pi^2 E}{3c}\sum_{\mu=x,y,z}\frac{dB(E;D_\mu^{E1})}{dE}. \tag{18}$$

C. Numerical details

1. Adaptive 3D grid representation

We employ a model space of 3D grid points inside a sphere of a radius $R_{\rm box}$. All the single-particle wave functions and potentials except for the Coulomb potential are assumed to vanish outside the sphere. For the calculation of the Coulomb potential, we follow the prescription in Ref. [19]. The differentiation is approximated by a finite difference with the nine-point formula.

In order to obtain nuclear response with a reasonable accuracy, we need a large model space, typically $R_{\rm box} \gtrsim$ 15 fm (see Sec. III B 1). This is much larger than the typical nuclear size R_0. Outside the nuclear radius R_0, we do not need to use a fine mesh. Thus we adopt an adaptive coordinate system to reduce the number of grid points in the outer region, $R_0 < r < R_{\rm box}$. We use the following coordinate transformation, $(u, v, w) \to (x, y, z)$, which was also adopted in Ref. [14],

$$x(u) = ku \left[1 + (k-1) \left\{ \frac{u}{x_0 \sinh(u/x_0)} \right\}^n \right]^{-1}, \quad (19)$$

and the same form for $y(v)$ and $z(w)$. In this transformation, we have $x(u) \approx u$ for spatial region of $u \ll x_0$, and $x(u) \approx ku$ for $u \gg x_0$. We adopt a uniform mesh spacing of $\Delta h = 0.8$ fm in the (u, v, w) space. The parameters, $k = 5.0$, $x_0 = 8$ fm, and $n = 2$, are used in the following calculations. The number of grid points in the sphere of $r \le R_{\rm box}$ is significantly reduced; $27,609 \to 11,777$ for $R_{\rm box} = 15$ fm and $221,119 \to 39,321$ for $R_{\rm box} = 30$ fm.

2. Choice of Iterative algorithms

In this section, we discuss performance of different iterative solvers to solve the linear response equations. We first discuss the calculation for the ground state. To obtain ground-state solutions, the imaginary-time iterative method is used [20]. We impose constraints in the iteration process so that the center-of-mass always coincides with the origin of the coordinate system and the principal axes of the density distribution coincide with three Cartesian axes of x, y, and z. It is important to obtain a well converged ground state solution, since the convergence properties of the linear-response calculation crucially depends on this. To assure the strict convergence in the ground state calculation, we impose the convergence condition not only for the total energy, but also for the deformation parameters (β, γ), single-particle energies ϵ_i, single-particle angular momenta, and so on.

For the Skyrme energy functional, the RPA matrix $\mathbf{A}$ which appears in Eqs. (6) and (7) is sparse in the $\vec{r}$-space grid representation. Therefore, the iterative methods, such as the conjugate gradient (CG) method [21], should work efficiently. The CG method is very powerful for the hermitian matrix. However, since we calculate for the complex frequency ω, the matrix $\mathbf{A}$ is no longer hermitian. Therefore, a simple CG method is not applicable. There are a lot of variants of the CG method extended for non-hermitian problems. We test some of them: Bi-conjugate gradient (Bi-CG) method [21], generalized conjugate residual (GCR) method [22], generalized product-type bi-conjugate gradient (GPBi-CG) method [23], Bi-CGSTAB method [24], and Bi-CGSTAB2 method [25]. In the original GCR method, it is necessary to store all the vectors $\vec{x}_0, \cdots, \vec{x}_{n-1}$ in order to calculate the vector at the n-th iteration. However, this is impractical because it requires heavy computational task and huge memory size. To avoid the problem, we restart the GCR procedure every twenty iterations. In Fig. 1, we show the convergence behavior of the different iterative solvers. The magnitude of the relative residue,

$$r_n = |\vec{b} - \mathbf{A}\vec{x_n}|/|\vec{b}| \quad (20)$$

is plotted against the number of iterations.

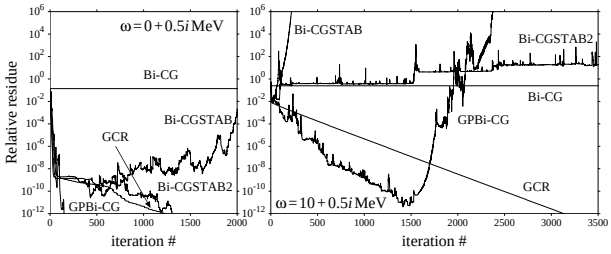

FIG. 1: Convergence property of different iterative methods to solve the linear response equations (6) and (7) for electric dipole response in ^{16}O calculated at complex frequencies of $\omega = 0 + 0.5i$ MeV (left) and $10 + 0.5i$ MeV (right). Relative residue, r_n, is shown as a function of iteration number n.

At very low energies ($\omega = 0 + 0.5i$ MeV), all the solvers except for the Bi-CG method provide quickly converged results. On the other hand, at higher energies ($\omega = 10 + 0.5i$ MeV), only the GCR and the GPBi-CG methods reach the convergence. In most cases, the convergence of the GPBi-CG method is faster than the GCR. However, after the convergence, the residue by the GPBi-CG method start to increase again. Therefore, only the result of the GCR method shows a stable convergence property in Fig. 1. We thus employ the GCR in the following calculations, although it has a disadvantage that it requires larger computer memory size than other methods based on the Bi-CG.

In the iteration procedure, we need to set up the initial vector $\vec{x}_0$. It turns out that the convergence property depends very little on the selection of the initial vector. We simply take the initial vector of $\vec{x}_0 = 0$. We stop the GCR iteration procedure if the relative residue becomes smaller than a threshold, $r_n < 10^{-6}$. We find the typical number of the iteration necessary to reach the convergence is about 10^3 around the excitation energy region of giant dipole resonance (GDR), while the

convergence is much faster for smaller $E(= \mathrm{Re}\,\omega)$. The iteration number to reach the convergence also depends on the imaginary part of the frequency, $\gamma(= 2\mathrm{Im}\,\omega)$, and is roughly proportional to $1/\gamma$.

We will later show how the convergence depends on other parameters. In the inset of Fig. 3, we show the residue, r_n of Eq. (20), as a function of the CPU time for calculations employing different spatial size $R_{\rm box}$. We can see that the computational time scales linearly both with the number of grid points and with the particle number A.

In Sec. III, the calculation is performed with the following settings, unless otherwise specified: The energy range of $0 \le E \le 38.1$ MeV, discretized in spacing of $\Delta E = 0.3$ MeV (128 points). The imaginary part of the frequency is fixed at 0.5 MeV, corresponding to $\gamma = 1.0$ MeV. The calculated strength is interpolated using the cubic spline function. In most cases, we have utilized PC cluster systems with either 64 or 128 processors in parallel.

3. Choice of the FAM parameter η

The FAM parameter η in Eq. (10) should be as small as possible to validate the linearity. In practice, there is a lower limit to avoid the round-off error. In the numerical computation, we use real variables with double precision (8 bytes) and complex variables with 8×2 bytes. We use the following value for η which differ for every iteration to ensure the linearity [15]:

$$\eta = \frac{\eta_{\rm Lin}}{\max\{N(X), N(Y)\}}, \quad N(\psi) = \frac{1}{A}\sqrt{\sum_{i=1}^{A}\langle\psi_i|\psi_i\rangle} \tag{21}$$

with $\eta_{\rm Lin} = 10^{-4}$. The convergence property of the GCR iteration is not sensitive to the value of $\eta_{\rm Lin}$, as far as the value is in the range of $\eta_{\rm Lin} = 10^{-2} - 10^{-6}$. However, if we use too small value, r_n oscillates in the iteration and never reaches the convergence.

III. CALCULATED RESULTS

A. Numerical accuracy

In this section, we demonstrate that the FAM, described in Sec. II, really works as a simple and accurate method for the fully self-consistent linear-response calculation with realistic Skyrme functionals. In Ref. [15], we have already done it for a simple Bonche-Koonin-Negele interaction [26].

In the following calculations, we use the Skyrme energy functional. We adopt the same functional form as that of Ref. [27] (Appendix A). In Ref. [27], every single-particle orbital is assumed to have a definite parity and z-signature symmetries. However, we do not assume any

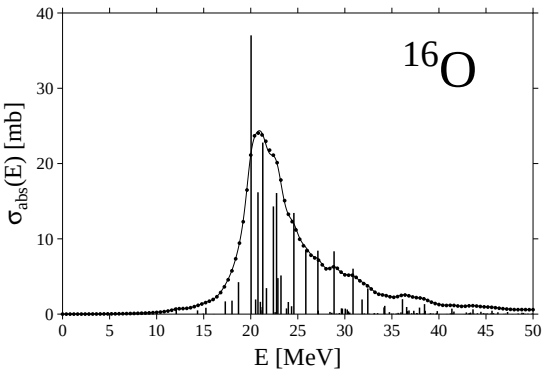

FIG. 2: Comparison of the results for electric dipole response of ^{16}O calculated by the present linear response formalism with FAM (dots) and by the eigenvalue formalism with an explicit construction of the residual interaction (curve). Both calculations use the cubic box of $(21\ \mathrm{fm})^3$ and the SIII functional. See text for details. The vertical lines indicate eigenenergies and strengths of the RPA normal modes calculated by the matrix diagonalization method, whose vertical magnitude is in units of mb·MeV.

of these in this paper. The functional depends on densities $\rho_\tau(\vec{r})$, kinetic densities $\tau_\tau(\vec{r})$, spin-orbit densities $\vec{J}_\tau(\vec{r})$, current densities $\vec{j}_\tau(\vec{r})$, and spin densities $\vec{\rho}_\tau(\vec{r})$, where $\tau = n$ and p. The exchange part of the Coulomb energy is evaluated by the Slater approximation. The center-of-mass correction is achieved by using the recoil nucleon mass, $M \to AM/(A-1)$.

In Fig. 2, we show photoabsorption cross section for ^{16}O calculated by two different methods: The dots are obtained by solving the linear response equations (6) and (7) in which the FAM is employed to evaluate the residual field. The vertical lines are obtained by the matrix diagonalization method [12, 13] in which the residual interaction taking a second derivative of the Skyrme energy function is constructed explicitly. The positions of the vertical lines indicate the energy eigenvalues, while the heights show the calculated cross section. The solid curve is obtained by smoothing the vertical lines with the energy-weighted Lorentzian. In both calculations of the linear response and the matrix diagonalization, the same Skyrme functional and the same grid representation of the $\vec{r}$-space are used. The width parameter is set common, $\gamma = 2$ MeV. In the matrix diagonalization method, the spurious solutions corresponding to the center-of-mass motion appear around a few tens keV. They are not shown in the figure.

This figure clearly demonstrates that the linear response calculation with the FAM denoted by dots completely agrees with the fully self-consistent RPA calculation with an explicit construction of the residual interaction. We should note that the computer program of the diagonalization method requires heavy and complicated coding for the residual interaction, while the program coding with the FAM can be achieved with the

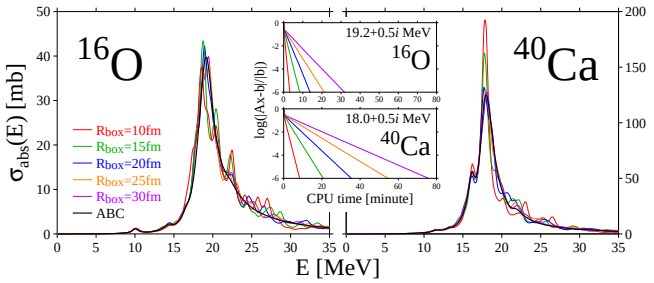

FIG. 3: Photoabsorption cross sections in ^{16}O and ^{40}Ca calculated with the FAM in a spherical box of different sizes: $R_{\rm box}$ = 10 fm, 15 fm, 20 fm, and 30 fm. "ABC" indicates a result with the absorbing boundary condition which properly treats the continuum effect [14]. The SkM* interaction and the smoothing parameter γ = 1 MeV are used. Inset: Convergence properties as a function of the CPU time.

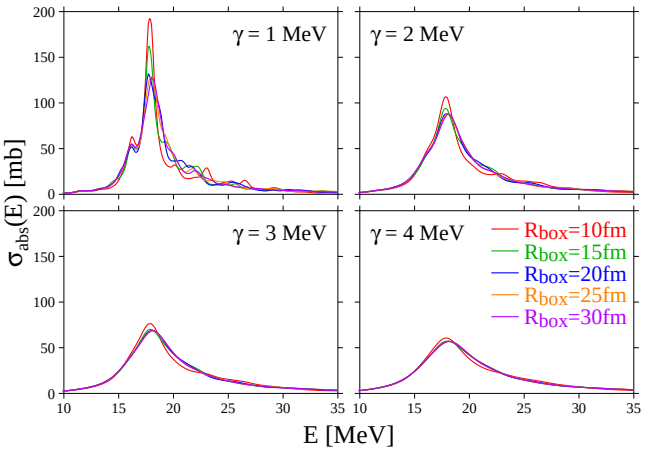

FIG. 4: Photoabsorption cross sections in spherical nucleus ^{40}Ca calculated with different $R_{\rm box}$ and with different γ values. The functional parameter set of SkM* is used.

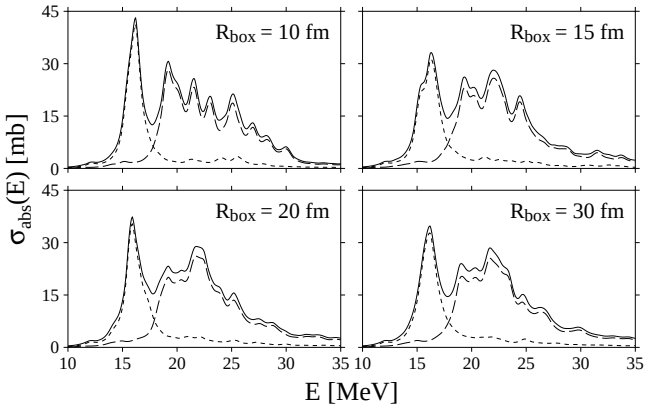

FIG. 5: Photoabsorption cross sections in deformed nucleus ^{24}Mg calculated with a spherical box of $R_{\rm box}$ = 10 fm, 15 fm, 20 fm, and 30 fm. Dashed, long dashed, and solid lines correspond to cross sections of K = 0 mode, K = 1 mode, and the total one, respectively. The functional parameter set of SkM* and the smoothing parameter γ = 1 MeV are used.

static mean-field calculation alone, with a minor modification. Thus the accuracy and the simplicity of the FAM is clearly demonstrated.

Let us next consider the merit of the linear response calculation for a fixed frequency in comparison with the matrix diagonalization method, apart from the FAM. In the matrix diagonalization method, the number of normal modes increases rapidly as the excitation energy becomes higher. Even when we assume the parity and the z-signature symmetries, the number of excited states is an order of one thousand in the energy range below 50 MeV. If we achieve matrix diagonalization in the mixed representation, we must calculate eigenvalues and eigenvectors of the RPA solution one by one. Then the calculations of a thousand of eigenstates require huge computational time. Therefore, to calculate responses for a wide energy region, the computation time with the linear response method is much smaller than that of the diagonalization method. Furthermore, we can easily parallelize the calculation in the linear response calculation, assigning different processors to solve the equation at different frequencies ω.

Combining these features, we consider the linear response calculation with the FAM is the best choice for the systematic, fully self-consistent calculations over a periodic table.

B. Light nuclei

1. *Dependence on box size and smoothing parameter*

We show how the results depend on the box size $R_{\rm box}$ and the smoothing parameter γ. In the present mixed representation, the model space is specified with $R_{\rm box}$ and the 3D mesh size Δh. The dependence on the mesh size is discussed in details in Ref. [12] for spurious and low-energy excitations in ^{16}O and ^{208}Pb. According to this study, $\Delta h \approx 0.8$ fm produces a converged result. In addition, we have also carefully examined the convergence with respect to the grid spacing in the adaptive-coordinate. We adopt $x_0 = 8$ fm in Eq. (19).

In Fig. 3, results of the calculations with $R_{\rm box}$ = 10, 15, 20, 25, and 30 fm are shown. As is seen in Fig. 3, small peaks in higher energies ($E > 20$ MeV) are disappearing with increasing $R_{\rm box}$. These small peaks at high energies are all spurious, due to the discretization of the continuum. In fact, the calculation with the proper continuum boundary condition [14], which is denoted as "ABC", shows only a smooth tail in this energy region above the main GDR peak. With the energy resolution of γ = 1 MeV, the effect of the discretized continuum is still

TABLE I: $R_{\rm box}$-dependence of the GDR peak positions and widths in units of MeV, for ^{16}O and ^{40}Ca. The smoothing parameter of $\gamma = 1$ MeV is used. See text for details.

^{16}O	$dB(E)/dE$		$\sigma_{\rm abs}(E)$	
	$E_{\rm peak}$	Γ	$E_{\rm peak}$	Γ
$R_{\rm box} = 10$ fm	18.993	3.869	18.798	3.876
$R_{\rm box} = 15$ fm	19.063	3.475	19.103	3.944
$R_{\rm box} = 20$ fm	19.141	3.096	19.151	3.435
$R_{\rm box} = 30$ fm	19.162	3.035	19.165	3.330
^{40}Ca	$dB(E)/dE$		$\sigma_{\rm abs}(E)$	
	$E_{\rm peak}$	Γ	$E_{\rm peak}$	Γ
$R_{\rm box} = 10$ fm	17.794	1.545	17.766	1.550
$R_{\rm box} = 15$ fm	17.797	2.334	17.796	2.492
$R_{\rm box} = 20$ fm	17.904	2.789	17.901	2.886
$R_{\rm box} = 30$ fm	17.963	2.956	17.959	3.014

visible at $E > 20$ MeV, even for the case of $R_{\rm box} \simeq 30$ fm. In order to remove the spurious effect, we need increase either $R_{\rm box}$ or γ. In Fig. 4, we show results for ^{40}Ca calculated with different box sizes and with different magnitudes of the smoothing parameter γ. Using $\gamma > 2$ MeV, the calculation roughly converges with $R_{\rm box} > 15$ fm. Thus, in the calculation with the vanishing (box) boundary condition, it is difficult to distinguish small physical peaks from unphysical ones in the high-energy continuum region, $E > 20$ MeV. In this article, we concentrate our discussion on gross structure of the main GDR peaks.

Next, in Fig. 5, we show results for ^{24}Mg. Since the ground state of ^{24}Mg is deformed with a prolate shape ($\beta_2 = 0.39$), the GDR splits into two major peaks, $K = 0$ mode (dashed line) and $K = 1$ mode (long dashed line). The $K = 0$ mode corresponds to the oscillation parallel to the symmetry axis (z direction) and $K = 1$ mode to that perpendicular to the symmetry axis (x and y directions). In the calculations with $R_{\rm box} = 10$ fm and 15 fm, we observe a peak at $E = 25$ MeV for the $K = 1$ mode. However, this peak becomes smaller for larger $R_{\rm box}$. This indicates that the peak at 25 MeV comes from the effect of the box discretization and is spurious.

Although the calculated profile functions of cross section in the high-energy continuum region are affected by the box discretization, the gross property of the GDR is less sensitive to the value of $R_{\rm box}$. We estimate the GDR peak energy and the width according to the electric dipole ($E1$) strength distribution and the photoabsorption cross section (oscillator strength distribution). For spherical nuclei, the nuclear response does not depend on the direction of the external dipole field. Thus, we can arbitrary choose it, for instance, $F = D_z^{E1}$. Then, $E1$ strength is fitted by a single Lorentzian function,

$$\frac{dB(E; D_z^{E1})}{dE} \approx B_{\rm tot} \times L(E),$$
$$L(E) = \frac{1}{\pi} \frac{\Gamma/2}{\left(E - E_{\rm peak}\right)^2 + (\Gamma/2)^2}, \qquad (22)$$

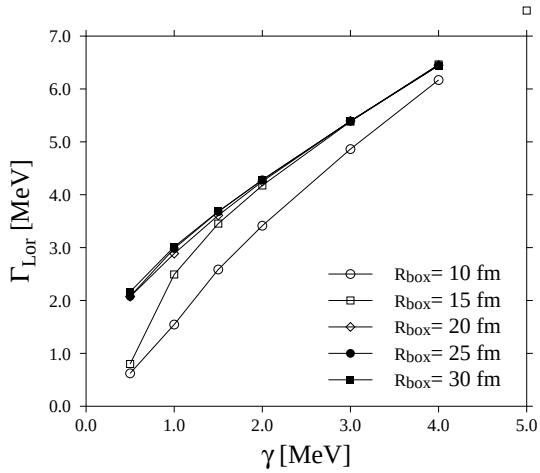

FIG. 6: Estimated GDR width for ^{40}Ca as a function of the parameter γ.

where $E_{\rm peak}$ and Γ are fitting parameters, and $B_{\rm tot} = \int dE dB(E)/dE$. The fitting is also performed for the photoabsorption cross section $\sigma(E)$, using the energy-weighted Lorentzian, $f_{\rm tot} \times EL(E)$. The results are shown in Table I. These two definitions of the peak energy and the width lead to nearly identical results.

The dependence of $E_{\rm peak}$ on the box size $R_{\rm box}$ is very small. On the other hand, the GDR width Γ shows a substantial dependence on the box size. For $\gamma = 1$ MeV, to estimate the width with a reasonable accuracy requires $R_{\rm box} > 20$ fm. However, the width also depends on the smoothing parameter γ, which is shown in Fig. 6. The value of Γ is converged at $R_{\rm box} \geq 20$ fm for $\gamma = 1$ MeV. When we use a larger γ value, the model space of $R_{\rm box} = 15$ fm is good enough to calculate the width. From the approximate linear dependence of Γ on the parameter γ, we can estimate the width at $\gamma = 0$ as $\Gamma^{\rm RPA} \approx 2$ MeV. This value can be regarded as the damping width in the RPA, namely due to the Landau damping and escaping: $\Gamma^{\rm RPA} = \Gamma^{\rm Landau} + \Gamma^{\uparrow}$. Since the smoothing parameter γ can be regarded as the spreading width, $\gamma = \Gamma^{\downarrow}$, we may extract $\Gamma^{\downarrow}$ from experimental data. This will be discussed in the followings.

2. *Comparison with experiments and Skyrme-functional dependence*

Calculated photoabsorption cross sections for spherical nuclei, ^{16}O, ^{40}Ca and deformed nucleus ^{24}Mg, are compared with experimental data in Fig. 7. The calculated energies of the GDR peaks are underestimated by a few MeV, but the overall structures are reproduced. For spherical nuclei, the GDR widths calculated with $\gamma = 1$ MeV are narrower than the corresponding experimental data. This seems to suggest that the spreading width $\Gamma^{\downarrow}$, which takes account of effects decaying into compound states, such as two-particle-two-hole excitations,

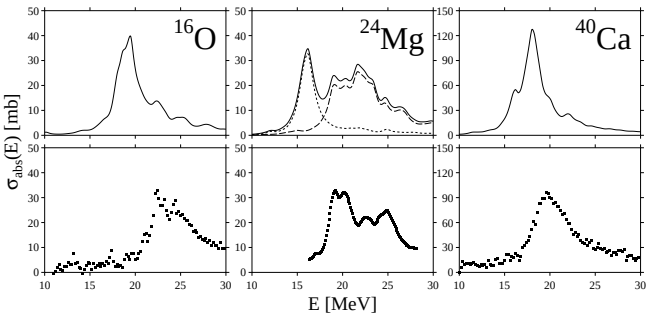

FIG. 7: Calculated (upper panels) and experimental (lower panels) [28, 29] photoabsorption cross sections in spherical nuclei ^{16}O, ^{40}Ca and deformed nucleus ^{24}Mg. We use the box size $R_{\rm box} = 30$ fm and the SkM* parameter set with $\gamma = 1$ MeV.

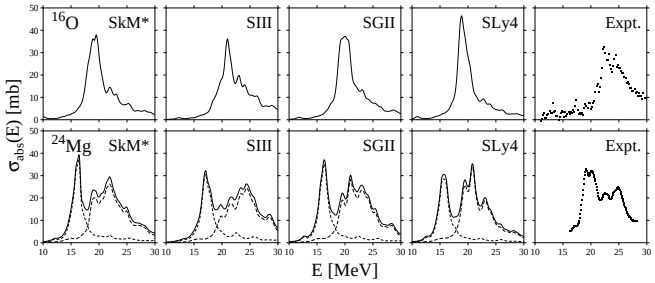

FIG. 8: Comparison of the calculated photoabsorption cross sections with different Skyrme parameter sets and experimental data in ^{16}O and ^{24}Mg. The calculation is performed with the box size $R_{\rm box} = 25$ fm.

is slightly larger than $\gamma = 1$ MeV. The cross section at higher energies is larger in experiment. This may be due to effect of the ground-state correlation produced by the tensor and short-range parts in the two-body nuclear interaction [18]. For ^{16}O, all the calculations fail to reproduce a double-peak structure of the GDR, present in experimental data. If we neglect the time-odd spin densities, the double peaks can be reproduced [14]. The GDR peak energy in ^{40}Ca is better reproduced compared to the case for ^{16}O. The calculated cross sections in the high-energy region also becomes closer to the experimental data. It seems that the discrepancy is more prominent for lighter nuclei.

For the deformed nucleus ^{24}Mg, the GDR peak splitting caused by the ground-state deformation well agree with the experiments, although the magnitude of the deformation splitting is slightly too large in the calculation. We may interpret that the experimental GDR peak around $E = 20$ MeV is associated with the $K = 0$ mode, and those at $E = 22 \sim 25$ MeV correspond to the $K = 1$ mode. The double-peak structure of the $K = 1$ GDR peak is well reproduced. Approximately, the calculated cross section is shifted to lower energy from the experimental ones, by about 3 MeV.

We next show results obtained with different Skyrme-parameter sets in Fig. 8; SkM* [30], SIII [31], SGII [32], and SLy4 [33]. Two parameter sets, SkM* and SLy4, produce similar results. In ^{16}O, the GDR peak position is calculated around $E = 19$ MeV. In contrast, the SIII functional produces the GDR peak near $E = 21$ MeV. The result with the SGII functional is intermediate, around $E = 20$ MeV. However, all the calculations underestimate the experimental GDR peak energy, $E \approx 22$ MeV. This discrepancy on the GDR peak energy will disappear for heavier nuclei (see Sec. III C). The cross section at higher energies $E > 25$ MeV is also systematically underestimated in the calculations. For deformed ^{24}Mg, all the calculations again underestimate the peak energies. Both of $K = 0$ and $K = 1$ peaks obtained with the SIII functional are located highest in energy compared to the others.

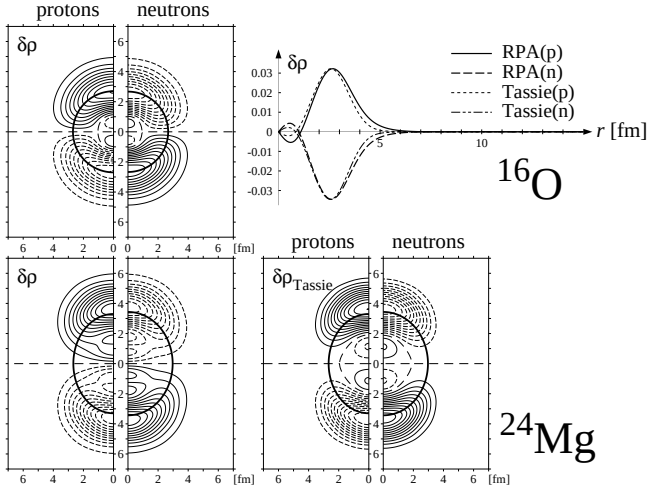

FIG. 9: Left panels: Contour maps of the calculated transition densities of $K = 0$ mode, $\mathrm{Im}\,\delta\rho(\omega)$, in the y-z ($x = 0$) plane at $\omega = 19.4 + 0.5i$ MeV in ^{16}O (upper panels) and $16.1 + 0.5i$ MeV in ^{24}Mg (lower). Contour lines with positive, negative, and zero values are denoted by solid, dashed, and long-dashed lines, respectively. Thick solid lines correspond to nuclear surface, defined by $y^2/\langle y^2\rangle + z^2/\langle z^2\rangle = 1$. Right panels: Transition densities predicted by the Tassie model. The magnitude is fitted to the RPA result at the maximum value. See text for details.

3. Transition density

We obtain the forward and backward amplitudes, $X_i(\xi,\omega)$ and $Y_i(\xi,\omega)$, using the FAM. Then, the local part of the transition density in the intrinsic frame, Eq. (3), can be calculated as

$$\delta\rho_\tau(\vec{r},\omega) = \sum_{i\in\tau}\sum_{\sigma}\left\{\phi_i^*(\xi)X_i(\xi,\omega) + Y_i^*(\xi,\omega)\phi_i(\xi)\right\}, \tag{23}$$

where $\tau = n$ or p. In this section, we adopt the external field of D_z^{E1} ($K = 0$). Using $\delta\rho(\omega)$ with $\omega = E + i\gamma/2$, the strength function can be written as

$$\begin{aligned}\frac{dB(E; D_z^{E1})}{dE} &= -\frac{1}{\pi}\mathrm{Im}\int d\vec{r} \\ &\quad \left(\frac{Ne}{A} z\delta\rho_p(\vec{r},\omega) - \frac{Ze}{A} z\delta\rho_n(\vec{r},\omega)\right) \\ &= \frac{2E\gamma}{\pi}\sum_n \frac{\tilde{E}_n |\langle n|D_z^{E1}|0\rangle|^2}{\left(E^2 - \tilde{E}_n^2\right)^2 + E^2\gamma^2}. \quad (24)\end{aligned}$$

Substituting $\langle n|D_z^{E1}|0\rangle$ by the following expression

$$\langle n|D_z^{E1}|0\rangle = \int d\vec{r}\frac{Ne}{A} z\langle n|\hat{\rho}_p(\vec{r})|0\rangle - \frac{Ze}{A} z\langle n|\hat{\rho}_n(\vec{r})|0\rangle, \quad (25)$$

we find

$$\mathrm{Im}\ \delta\rho_{n(p)}(\vec{r},\omega) \propto \sum_n \frac{\tilde{E}_n \langle 0|D_z^{E1}|n\rangle\langle n|\hat{\rho}_{n(p)}(\vec{r})|0\rangle}{\left(E^2 - \tilde{E}_n^2\right)^2 + E^2\gamma^2}, \quad (26)$$

where $\hat{\rho}_\tau(\vec{r}) = \sum_{i\in\tau}\delta(\vec{r} - \vec{r}_i)$. If there is a single state $|n\rangle$ that gives a dominant contribution in the vicinity of $E = \tilde{E}_n$ (within the width of γ), we have Im $\delta\rho(\omega) \propto \langle n|\hat{\rho}|0\rangle$.

The left panels of Fig. 9 show the calculated transition densities of neutrons and protons separately, at $\omega = 19.4 + 0.5i$ MeV for ^{16}O and at $\omega = 16.1 + 0.5i$ MeV for the $K = 0$ mode of ^{24}Mg. These energies correspond to the peak energies of the GDR. In the transition density of ^{16}O, one can clearly see the isovector character. In the top-right panel of Fig. 9, we show $\partial\rho_0/\partial r$ for ^{16}O, where the $\rho_0(r)$ is the ground-state density profile. This corresponds to the transition density predicted by the Tassie model for an irrotational and incompressible fluid. As is discussed in the literatures [3], the GDR of light nuclei is approximately represented by this classical fluid model. On the other hand, the transition density of ^{24}Mg shows more complicated features. We show, in the bottom-right panel of Fig. 9, a contour plot of the transition density in the Tassie model, $\delta\rho \propto \nabla\rho_0 \cdot \nabla r Y_{10}(\hat{r}) \sim \partial\rho_0/\partial z$. Compared to the RPA transition density, there is a deviation, especially in the nodal structure in the interior region. This may suggest the importance of coupling of the dipole mode to the octupole and higher-multipole modes.

C. Heavy nuclei

For heavier nuclei, the calculation better agrees with experiments. As is well-known, in heavy spherical nuclei, a single energy-weighted Lorentzian curve can fit the experimental data of the photoabsorption cross section very well [34]. We calculate photoabsorption cross sections in spherical nuclei ^{90}Zr, ^{120}Sn, and ^{208}Pb within a box of radius $R_{\mathrm{box}} = 15$ fm and compare them with experimental data in Fig. 10. The calculated GDR peak shows a splitting, however, this may be due to the spurious effect coming from the box discretization. Except for this splitting, the results agree well with the experimental data. Table II shows the calculated and the experimental values of the GDR peak positions and the widths. Both values are extracted from the Lorentzian fit to the photoabsorption cross section. According to Ref. [34], the Lorentzian function of the form (16),

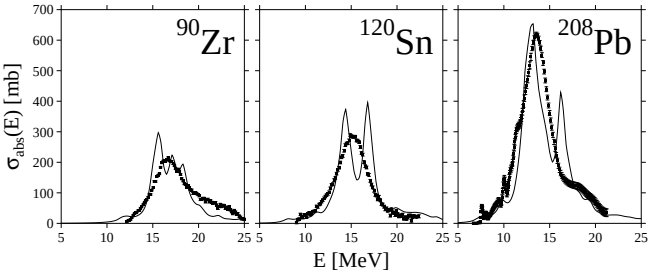

FIG. 10: Calculated photoabsorption cross sections for ^{90}Zr, ^{120}Sn, and ^{208}Pb. The calculation has been performed with $R_{\mathrm{box}} = 15$ fm, the SkM* parameter set, and $\gamma = 1$ MeV. The experimental data (symbols) are taken from Refs. [37–39].

$$\sigma_{\mathrm{abs}}(E) = \frac{\sigma_0}{1 + (E^2 - E_{\mathrm{peak}}^2)^2/(E^2\Gamma^2)}, \quad (27)$$

is used. The GDR peak positions are well reproduced within an error of 400 keV. The systematic deviation of the peak energies, seen in calculations for light nuclei, cannot be observed for these heavy systems. Therefore, we may conclude that the SkM* functional reproduces peak energies of the $E1$ resonances in heavy nuclei.

The calculated widths are slightly smaller than the experiments, by 300 $\sim$ 700 keV. Since we use $\gamma = 1$ MeV in these calculations, this indicates the spreading width of $\Gamma^\downarrow = 1.3 \sim 1.7$ MeV. The total damping width is about 4 MeV for these nuclei. Thus, the spreading width is less than half of the total width. This is rather surprising because, for heavy nuclei, the spreading width was supposed to be a major part of the total damping width [35, 36]. However, the fragmentation of the strength into non-collective 1p-1h states (Landau damping), which can be described by the RPA theory, is significant for these heavy systems. Thus, the spreading width of $\Gamma^\downarrow \sim 1.5$ MeV is able to reproduce a broadening of the experimental strength distribution. This observation seems consistent with recent self-consistent RPA calculations for spherical nuclei [5, 7].

IV. CONCLUSIONS

We have presented an implementation of the finite amplitude method (FAM) to make a fully self-consistent

TABLE II: Calculated and experimental [34] GDR peak energies and widths for ^{90}Zr, ^{120}Sn, and ^{208}Pb. The FAM calculation was performed with the same parameter set as Fig. 10.

	Calculation		Experiment	
Nucleus	$E_{\rm peak}$ [MeV]	Γ [MeV]	$E_{\rm peak}$ [MeV]	Γ [MeV]
^{90}Zr	16.37	3.85	16.74	4.16
^{120}Sn	15.22	4.52	15.40	4.89
^{208}Pb	13.26	3.47	13.63	3.94

RPA calculation employing a realistic Skyrme energy functional. Although the RPA is a well established theory and have been widely applied, a fully self-consistent calculation with a realistic functional is rather limited. This is mostly because of the complexity to construct the residual two-body kernels for realistic functionals. The FAM, which was proposed recently by the present authors, makes it possible to achieve a fully self-consistent RPA calculation without an explicit construction of the residual two-body kernels. Instead, the residual fields are evaluated by the finite difference, employing a computational code for the static mean-field Hamiltonian alone with a minor modification.

We implemented the FAM in the mixed representation where the orbital indices are used for the occupied orbitals while the three-dimensional Cartesian grid points are used for the unoccupied orbitals. In this representation, the linear response equation is a linear algebraic problem with a sparse and non-hermitian matrix. We have tested several solvers for the problem, and have found that the generalized conjugate residual method works stably to obtain the solution. We also examined the accuracy of the FAM employing a different parameters of the finite difference, and have found that the method works robust, namely, accurate results can be obtained for a certain wide range of finite difference parameter.

We show results of the fully self-consistent RPA calculation for the electric dipole responses of several nuclei of spherical and deformed shapes. For light nuclei, we have found a systematic underestimation of the average excitation energy, irrespective of the energy functional employed. We further notice the underestimation of the strength above the giant dipole resonance. The discrepancy is significant only for light nuclei, the average excitation energies of heavy nuclei are reasonably described. For a deformed nucleus ^{24}Mg, the calculation shows a deformation splitting of the giant dipole resonance, which well agrees with measurements. For spherical heavy nuclei, we have found a substantial part of the width can be explained within the RPA, leaving less than half of the total width for a spreading width, in contrast to the previous studies which reported that most of the width is attributed to the spreading mechanism for heavy nuclei.

We are currently performing a systematic calculation of the electric dipole responses for light to medium mass nuclei using the present method and Skyrme energy functionals. In a forthcoming paper, we will report a systematic analysis of the properties of the giant dipole resonance, including the average excitation energy, width, and the low-lying dipole mode around the threshold.

Acknowledgments

This work is supported by Grant-in-Aid for Scientific Research on Innovative Areas (No. 20105003) and by the Grant-in-Aid for Scientific Research(B) (No. 21340073). Computational resources were provided by the PACS-CS project and the Joint Research Program (07b-7, 08a-8, 08b-24) at Center for Computational Sciences, University of Tsukuba, by the Large Scale Simulation Program (Nos. 07-20 (FY2007), 08-14 (FY2008)) of High Energy Accelerator Research Organization (KEK). Computations were also performed on the RIKEN Super Combined Cluster (RSCC). We also thank the International Research Network for "Exotic Femto Systems" (EFES) of the Core-to-Core Programs of JSPS and the UNEDF SciDAC collaboration.

[1] D. Lunney, J. M. Pearson, and C. Thibault, Rev. Mod. Phys. **75**, 1021 (2003).
[2] M. Stoitsov, J. Dobaczewski, W. Nazarewicz, S. Pittel, and D. Dean, Phys. Rev. C **68**, 054312 (2003).
[3] P. Ring and P. Schuck, *The nuclear many-body problems*, Texts and monographs in physics (Springer-Verlag, New York, 1980).
[4] J. Terasaki, J. Engel, M. Bender, J. Dobaczewski, W. Nazarewicz, and M. Stoitsov, Phys. Rev. C **71**, 034310 (pages 15) (2005).
[5] J. Terasaki and J. Engel, Phys. Rev. C **74**, 044301 (pages 19) (2006).
[6] S. Fracasso and G. Colò, Phys. Rev. C **72**, 064310 (2005).
[7] T. Sil, S. Shlomo, B. K. Agrawal, and P.-G. Reinhard, Phys. Rev. C **73**, 034316 (2006).
[8] N. Paar, P. Ring, T. Nikšić, and D. Vretenar, Phys. Rev. C **67**, 034312 (2003).
[9] S. Péru and H. Goutte, Phys. Rev. C **77**, 044313 (2008).
[10] D. P. Artega and P. Ring, Phys. Rev. C **77**, 034317 (2008).
[11] K. Yoshida and N. V. Giai, Phys. Rev. C **78**, 064316 (2008).
[12] H. Imagawa and Y. Hashimoto, Phys. Rev. C **67**, 037302 (2003).
[13] T. Inakura, H. Imagawa, Y. Hashimoto, S. Mizutori, M. Yamagami, and K. Matsuyanagi, Nucl. Phys. A **768**, 61 (2006).
[14] T. Nakatsukasa and K. Yabana, Phys. Rev. C **71**, 024301 (pages 14) (2005).
[15] T. Nakatsukasa, T. Inakura, and K. Yabana, Phys. Rev.

C **76**, 024318 (pages 9) (2007).
[16] S. Shlomo and G. Bertsch, Nucl. Phys. A **243**, 507 (1975).
[17] R. H. Lemmer and M. Vénéroni, Phys. Rev. **170**, 883 (1968).
[18] A. Bohr and B. R. Mottelson, *Nuclear Structure, Vol. II* (W. A. Benjamin, New York, 1975).
[19] H. Flocard, S. E. Koonin, and M. S. Weiss, Phys. Rev. C **17**, 1682 (1978).
[20] K. T. R. Davies, H. Flocard, S. Krieger, and M. S. Weiss, Nucl. Phys. A **342** (1980).
[21] W. H. Press, S. A. Teukolsky, W. T. Vetterling, and B. P. Flannery, *Numerical Recipes in C* (Cambridge University Press, New York, 2007).
[22] S. C. Eisenstat, H. C. Elman, and M. H. Schultz, SIAM J. Numer. Anal. **20**, 345 (1983).
[23] S.-L. Zhang, SIAM J. Sci. Comput. **18**, 537 (1997).
[24] H. A. V. der Vorst, SIAM J. Sci. Stat. Comput. **13**, 631 (1992).
[25] M. H. Gutknecht, SIAM J. Sci. Comput. **14**, 1020 (1993).
[26] P. Bonche, S. Koonin, and J. W. Negele, Phys. Rev. C **13**, 1226 (1976).
[27] P. Bonche, H. Flocard, and P. H. Heenen, Nucl. Phys. A **467**, 115 (1987).
[28] M. A. Elkin, B. S. Ishkhanov, I. M. Kapitonov, E. I. Lileeva, and E. V. Shirokov, Physics of Atomic Nuclei **67** (2004).
[29] V. V. Varlamov, M. E. Stepanov, and V. V. Chesnokov, Bull. Rus. Acad. Sci. Phys. **67**, 724 (2003).
[30] J. Bartel, P. Quentin, M. Brack, C. Guet, and H. Håkansson, Nucl. Phys. A **386**, 79 (1982).
[31] M. Beiner, H. Flocard, N. van Giai, and P. Quentin, Nucl. Phys. A **238**, 29 (1975).
[32] N. van Giai and H. Sagawa, Nucl. Phys. A **371**, 1 (1981).
[33] E. Chanbanat, P. Bonche, P. Haensel, J. Mayer, and R. Schaeffer, Nucl. Phys. A **627**, 710 (1997).
[34] B. L. Berman and S. C. Fultz, Rev. Mod. Phys. **47**, 713 (1975).
[35] J. Wambach, Rep. Prog. Phys. **51**, 989 (1988).
[36] M. N. Harakeh and A. van der Woude, *Giant resonances*, Oxford Studies in Nuclear Physics 24 (Oxford University Press, Oxford, 2001).
[37] H. B. A. Leprêtre and, R. Bergère, P. Carlos, A. Veyssière, and M. Sugawara, Nucl. Phys. A **175**, 609 (1971).
[38] A. Leprêtre, H. Beil, R. Bergère, P. Carlos, A. D. Miniac, A. Veyssière, and K. Kernbach, Nucl. Phys. A **219**, 39 (1974).
[39] S. N. Beljaev and V. A. Semenov, Izv. Ross. Akad. Nauk, SSSR, Ser. Fiz. **55(5)**, 953 (1991).